Article



Heterogeneity Profoundly Alters Emergent Stress Fields in Constrained Multicellular Systems

Zachary E. Goldblatt, ¹ Habibeh Ashouri Choshali, ² Heather A. Cirka, ¹ Vivian Liang, ¹ Qi Wen, ³ Dannel McCollum, ⁴ Nima Rahbar,² and Kristen L. Billiar¹,⁷

¹Department of Biomedical Engineering, ²Department of Civil Engineering, and ³Department of Physics, Worcester Polytechnic Institute, Worcester, Massachusetts; and ⁴Department of Biochemistry & Molecular Pharmacology, University of Massachusetts Medical School, Worcester, Massachusetts

ABSTRACT Stress fields emerging from the transfer of forces between cells within multicellular systems are increasingly being recognized as major determinants of cell fate. Current analytical and numerical models used for the calculation of stresses within cell monolayers assume homogeneous contractile and mechanical cellular properties; however, cell behavior varies by region within constrained tissues. Here, we show the impact of heterogeneous cell properties on resulting stress fields that guide cell phenotype and apoptosis. Using circular micropatterns, we measured biophysical metrics associated with cell mechanical stresses. We then computed cell-layer stress distributions using finite element contraction models and monolayer stress microscopy. In agreement with previous studies, cell spread area, alignment, and traction forces increase, whereas apoptotic activity decreases, from the center of cell layers to the edge. The distribution of these metrics clearly indicates low cell stress in central regions and high cell stress at the periphery of the patterns. However, the opposite trend is predicted by computational models when homogeneous contractile and mechanical properties are assumed. In our model, utilizing heterogeneous cell-layer contractility and elastic moduli values based on experimentally measured biophysical parameters, we calculate low cell stress in central areas and high anisotropic stresses in peripheral regions, consistent with the biometrics. These results clearly demonstrate that common assumptions of uniformity in cell contractility and stiffness break down in postconfluence confined multicellular systems. This work highlights the importance of incorporating regional variations in cell mechanical properties when estimating emergent stress fields from collective cell behavior.

SIGNIFICANCE Mechanical stress fields within tissues generated by force transmission between cells play a critical role in cell behaviors ranging from proliferation to differentiation to death. The intracellular stresses are currently calculated using computational models assuming homogeneous mechanical properties. When applied to dense cell monolayers with geometrically constrained growth, these models predict distributions of stresses that are inconsistent with experimentally measured stress-related biological markers. Here, using a series of finite element models with experimentally measured heterogeneous cell material properties, we compute stresses that strongly correlate with a wide range of biophysical markers. Our results demonstrate that an understanding of the underlying mechanics that regulate collective cell behavior in dynamic biological tissues requires analyses of the heterogeneity of the cell material properties.

INTRODUCTION

Emergent mechanical stress fields arising from force transmission between cells in monolayers and multicellular aggregates are increasingly being recognized as major contributors to the regulation of collective cell behavior. Diffusion of growth factors and cytokines are not sufficient

Submitted July 12, 2019, and accepted for publication November 5, 2019.

*Correspondence: kbilliar@wpi.edu

Editor: Guy Genin.

https://doi.org/10.1016/j.bpj.2019.11.018

© 2019 Biophysical Society.

to explain the diversity seen in behaviors of cells just microns apart. Emergent stress fields have been studied in the context of proliferation (1), differentiation (2,3), nuclear transcription factor localization (4), tumorigenicity (5), cellular alignment (6,7), and collective migration speed (8). There is growing evidence that mechanical stress fields are pivotal in controlling these events.

There is considerable interest in quantifying the cellular stresses within monolayers to better understand the mechanical factors that drive migration, proliferation, and differentiation. For forward predictions of emergent stress fields,



researchers use continuum models with prestrain or finite element models with thermal cooling to simulate active cell contraction (1,2,7,9). To calculate cell-layer stress fields from measured substrate traction forces, monolayer stress microscopy (MSM) (10) and other force balancing methods (6,11–13) have been developed.

Calculation of stresses within a cluster of cells requires assumptions about the isotropy, thickness, elastic constants, and uniformity of the cell layer (14). In both predictions and calculations of cell-layer stress, the mechanical properties of cells are assumed to be uniform in past studies. Assumptions of material homogeneity may be acceptable for cell monolayers in which unconstrained migration and spreading results in regional uniformity in cell density and orientation (15); however, in constrained systems (e.g., micropatterned protein islands in vitro and tissues with confined growth in vivo), regional differences in cell behavior markers indicative of variations in cell properties are commonly reported. Higher rates of proliferation (2), increased circumferential alignment (6), enhanced tumorigenicity (5), and heightened contractility markers (2,16) are reported near multicellular system edges compared to central regions (1-3).

Here, we test the hypothesis that incorporation of heterogeneous mechanical parameters in calculations and simulations are necessary to accurately determine cell-layer stresses in geometrically constrained multicellular systems. We culture cells on micropatterned collagen islands to postconfluence and measure a broad range of biophysical markers indicative of cell stress state. We then predict and compute in-plane cell stress distributions using thermal contraction finite element models and MSM. The models are run with homogeneous and heterogeneous assumptions of cell-layer contractility and elastic modulus based on cell spread area, indentation stiffness, and traction force measurements.

MATERIALS AND METHODS

Cell culture

Valvular interstitial cells (VICs) were isolated from porcine hearts obtained from a local abattoir (17). Cells were expanded and cultured in Dulbecco's Modified Eagle Medium (4.5 g/L glucose; Life Technologies, Grand Island, NY), supplemented with 10% fetal bovine serum (GE Healthcare Life Sciences, Chicago, IL) and 1% antibiotic/antimycotic (Life Technologies). Cells were maintained in a temperature- (37°C), CO₂- (5%), and humidity-regulated incubator. Passages 2–6 were used for all experiments. VICs were seeded at 2000 and 10,000 cells/cm² for low cell density experiments of individual cells and high cell density experiments of aggregates, respectively, and allowed to adhere overnight. Media was changed after 24 h to remove any nonadhered cells. Aggregates were cultured for 48 h before traction force microscopy measurements.

Microcontact substrate preparation

Polyacrylamide gels (~40 kPa modulus) were attached to glass coverslips and used as the substrate for all experiments. Formulations of polyacryl-

amide/bisacrylamide to known mechanical modulus had been previously validated in a prior study (18). Individual cell studies used polyacrylamide gels coated with monomeric collagen by functionalization of the surface using Sulfo-SANPAH (Thermo Fischer Scientific, Waltham, MA). Multicellular aggregate studies used polyacrylamide gels that were microcontact printed with monomeric collagen using polydimethylsiloxane stamps of $200\text{-}400~\mu\text{m}$ diameter circular posts, as previously described (16).

Live cell imaging

CellEvent Caspase-3/7 reagent (Thermo Fisher Scientific) was added to cultures and allowed to incubate for 1 h before imaging. Phase images of aggregates and fluorescent images of caspase signal were obtained using a Zeiss Axiovert 200 M microscope (Oberkochen, Germany) equipped with a CCD camera, AxioVision software (Zeiss), and a 40× Zeiss objective. A custom MATLAB (The MathWorks, Natick, MA) program was developed for image processing to determine regional caspase location.

Traction force microscopy

Polyacrylamide gels were prepared and uniformly coated with $0.2~\mu m$ fluorescent beads (Life Technologies) as previously described (19). Images of aggregates were taken in phase contrast. Hoechst (Thermo Fisher Scientific) was added to media, incubated for 15 min, and imaged to count the number of cells within each aggregate. Fluorescent images of the substrate were taken before and after the addition of trypsin. Aggregate substrate traction data were obtained by calculating stresses in ANSYS (Ansys, Canonsburg, PA) from displacement fields that were computed using mass particle image velocimetry from a custom MATLAB code (19).

Atomic force microscopy

Atomic force indentation stiffness was measured for individual VICs cultured on compliant substrates of varying moduli. For each cell, a $20\times20~\mu m$ force map was completed over the cell body. The indentation rate was 1 $\mu m/s$ (0.06 N/m cantilever, conical tip; Asylum Research, Santa Barbara, CA). 16 measurements comprised each map. A custom MATLAB script was then used to extract the Young's modulus from each curve by fitting the first 200 nm of indentation data to the Hertz model for a conical indenter. The extracted values were averaged to determine the mean modulus for each cell. A similar experimental technique was used for aggregates in which $20\times20~\mu m$ force maps were produced over the center and edge of the aggregates. One map in each category was performed per aggregate. Data analysis was identical to that of individual cells.

Immunocytochemistry

To determine the distribution of the various biometric markers, cells were fixed with 4% paraformaldehyde and permeabilized with 0.25% Triton-X (Millipore Sigma, Burlington, MA). Visualization of G-actin was accomplished by staining VICs with deoxyribonuclease I, Alexa Fluor 594 conjugate (Life Technologies) for 30 min. Cells were counterstained for filamentous actin (F-actin) with Alexa Fluor 488 phalloidin (Thermo Fisher Scientific) and Hoechst diluted in phosphate-buffered saline (PBS), also for 30 min. The intensities were compared between the G-actin channel and Factin channel to generate a ratio for all cells and aggregates. An F-actin alignment index was determined by processing phalloidin-stained actin images with a two-dimensional (2D) fast Fourier transform on sequential 8 μ m subimages. The F-actin alignment index was then calculated as one minus the ratio of minor/major axes of the fitted ellipse from the thresholded fast Fourier transform image. An index of zero indicates no stress fiber alignment, and a value of 1 indicates perfect fiber alignment. α -SMA-stained cells were first blocked with 1.5% goat serum (Invitrogen, Carlsbad, CA) and then stained for α-SMA (Sigma-Aldrich, St. Louis, MO). Confocal imaging was completed on a Leica SP5 microscope (Leica Microsystems, Wetzlar, Germany) using the same laser intensities for all samples.

Modeling

A schematic outlining the different stress components as well as the different models can be found in Fig. S1.

Thermal contraction model

A three-dimensional (3D) finite element model of the cell layer and substrate was constructed using the commercial software Abaqus (Dassault Systémes, Vélizy-Villacoublay, France). The cell layer is modeled as a continuous 3D layer where the contractility is simulated with a temperature drop equivalent to applying a uniform prestrain. The constitutive equation for the isotropic cell layer is the same as the thermoelasticity equation as

$$\sigma_{ij} = \frac{E_c}{1 + \nu_c} \left(\varepsilon_{ij} + \frac{\nu_c}{1 - 2\nu_c} \varepsilon_{kk} \delta_{ij} \right) - \frac{E_c}{1 - 2\nu_c} \alpha \Delta T \delta_{ij}, \quad (1)$$

where, E_c is elastic modulus, ν_c is Poisson's ratio, α is the coefficient of thermal expansion, ΔT is the temperature change, δ_{ii} is the Dirac delta function, and σ_{ii} and ε_{ii} are the stress and strain fields, respectively, which are obtained numerically using finite element methods.

Cell-layer contraction was modeled by introducing a thermal strain using a temperature drop of 1 K. The thickness of cells and substrate layers were 3.2 and 1 μ m, respectively; the bottom surface of the substrate was fixed. The cell layer and substrate layer were modeled as elastic, isotropic materials with Young's moduli of 40 and 0.4 kPa, respectively, both with a Poisson's ratio of 0.49 (nearly incompressible). The substrate layer undergoes a softening effect caused by the inclusion of the adhesive bonding layer between the cell layer and the substrate. A two-spring model was used to acquire the effective stiffness of the substrate and molecular bond based on values from Ji and colleagues (7). We performed a parametric study showing the sensitivity of substrate stiffness on cell stress distribution and found that the qualitative results do not change over three orders of magnitude of the chosen modulus (i.e., 0.04-4 kPa). The quantitative values do change but are normalized to radius and stress because the overall level of contraction set by the thermal coefficient and temperature drop is arbitrary (Fig. S2). In the first model iteration, the modulus was assumed uniform to highlight the effect of varying contractility. A second parametric study was performed showing that both contractility and substrate modulus affect stress distribution independently from one another (Fig. S3).

The coefficient of thermal expansion, α , was set to the exponential function $\alpha'(r) = 0.9e^{2.34r}$ for the exponential heterogeneous case based on the relationship of cell area versus aggregate radius, r. This equation was normalized to its maximum value at r = R, the maximum radius, and multiplied by 0.1 to achieve an $\alpha=0.1~\text{K}^{-1}$ at the aggregate edge based off of values from Ji and colleagues (7), yielding Eq. 2 as follows:

$$\propto (r) = \frac{0.9e^{2.34r}}{0.9e^{2.34R}} x \ 0.1 = 0.0096e^{2.34r}. \tag{2}$$

The values for α in each condition were normalized to each other so that the area under each α versus radius curve remains equivalent. This causes the α values for the homogeneous cell layer to be 0.0357 K⁻¹. For the step heterogeneity case, the α value in the peripheral region (r > 0.5R) was set to be 0.0476 K⁻¹, and the α value in the central region was set to be 0.0238 K^{-1} , that is, the center was half as contractile as the edges.

For the simulation, the radius of the substrate was 400 μ m, and the radius of the cell layer was 200 μ m. Standard 3D-stress hexahedral elements with an approximate global mesh size of 2 μ m were used. Stress and strain tensors were calculated throughout the model, and the radial and circumferential cell-layer stresses at the cell-substrate interaction were reported. Consistent with previous simulations (1), we assumed uniform focal adhesions between the cell layer and substrate layer to focus on only one variable (contractility). Localization of focal adhesions varies by region within aggregates and is likely higher at aggregate edges (20-22); however, they are still present within the central region (just not as dense or large). We performed a simulation in which only a thin ring (5 μ m thick) around the edge of the cell layer is attached to the substrate layer, simulating focal adhesions only at the aggregate edge. In this case, the circumferential stresses are slightly accentuated as they progress toward the aggregate edge, yet the qualitative stress distributions remain consistent with the uniform attachment case (Fig. S4).

MSM. The in-plane stresses in the cell layer were calculated using experimentally measured tractions. The displacement field from traction force microscopy was applied to a semi-infinite substrate with Young's modulus of 40 kPa and the tractions were obtained. A 2D finite element model of the cell layer was constructed using Abaqus, in which tractions were applied to the bottom surface of the cell layer. The cell layer is modeled as a continuous flat, thin layer under plane-stress conditions such that all out-of-plane stress/traction components are negligible ($\sigma_{zz}=\sigma_{rz}=\sigma_{\theta z}=T_z=0$). Under static conditions, the 2D equilibrium equations in polar coordinates are as follows:

$$\frac{\partial \sigma_{rr}}{\partial r} + \frac{1}{r} \frac{\partial \sigma_{r\theta}}{\partial \theta} + \frac{1}{r} (\sigma_{rr} - \sigma_{\theta\theta}) = \frac{T_r}{t_c} \text{ and}$$
 (3)

$$\frac{\partial \sigma_{r\theta}}{\partial r} + \frac{1}{r} \frac{\partial \sigma_{\theta\theta}}{\partial \theta} + \frac{2}{r} \sigma_{r\theta} = \frac{T_{\theta}}{t_{c}},\tag{4}$$

where T_r and T_{θ} are the measured radial and circumferential traction components, respectively, applied to the lower surface of the model, r is the radius, σ_{ii} are the stress components, and t_c is the monolayer thickness.

The general form for Hook's law in standard tensor notation is expressed as follows:

$$\sigma_{ij} = C_{ijkl} \varepsilon_{kl}. \tag{5}$$

When under homogeneous, isotropic plane stress, the above equation in polar coordinates can be simplified as follows:

$$\varepsilon_{rr} = \frac{1}{E} (\sigma_{rr} - \nu \sigma_{\theta\theta}), \tag{6}$$

$$\varepsilon_{\theta\theta} = \frac{1}{E} (\sigma_{\theta\theta} - v\sigma_{rr}), \text{ and}$$
(7)

$$\varepsilon_{r\theta} = \frac{1+v}{E}(\sigma_{r\theta}). \tag{8}$$

Then, the compatibility equation for plane stress in polar coordinates is

$$\nabla^{2}(\sigma_{rr} + \sigma_{\theta\theta}) = \frac{(1+v)}{t_{c}} \left(\frac{\partial T_{r}}{\partial r} + \frac{T_{r}}{r} + \frac{1}{r} \frac{\partial T_{\theta}}{\partial \theta} \right) \text{ and }$$
 (9)

$$\nabla^2 = \frac{\partial^2}{\partial r^2} + \frac{1}{r} \frac{\partial}{\partial r} + \frac{1}{r^2} \frac{\partial^2}{\partial \theta^2}.$$
 (10)

The stresses are numerically calculated. The standard plane-stress fournode element was used to mesh the cell layer with an approximate mesh size of 1.5 μ m. Homogeneous, step heterogeneous, and exponential

heterogeneous cell properties were considered. For the exponential case, an elastic modulus was exponentially increased from the center to the edge using the function $E(r) = 0.9e^{2.34r}$, such that the modulus at the edge was E =40 kPa. Similar to the calculations for α , the values for the moduli in each condition were normalized so the area under each modulus versus radius curve remains equal. With the elastic modulus of the exponential case set to 40 kPa at the aggregate edge, the modulus of the homogeneous case is reduced to 18.6 kPa, whereas for step heterogeneity, the moduli were 12.5 and 24.9 kPa for the central region (r < 0.5R) and peripheral region, respectively. This modulus range is within values for average cell-layer stiffness found in our atomic force microscopy (AFM) experiments. The tractions at the cell-layer nodes corresponding to the model mesh were found by interpolation of the tractions at the substrate nodes. The radial and circumferential stresses in the cell layer were reported.

Magnetic induction of stress

To apply external forces to the cells within a subset of aggregates, ferrous beads were attached to the cells and a magnetic force was applied. Ferric oxide microbeads (5 µm diameter; Sigma-Aldrich) were mixed vigorously and allowed to incubate in collagen solution prepared by mixing 1 mg/mL collagen (Advanced BioMatrix, Carlsbad, CA) with 10% 0.1 M NaOH to achieve a pH of 7.4 for 1 h to ensure proper collagen coating on the beads. The solution was then spun down, supernatant aspirated, and beads were resuspended in Dulbecco's PBS. Before application onto aggregates, the microbeads were sonicated for an additional 10 min to reduce clumping. The microbead mixture was added to new cell media (1:100 v/v) for aggregates that had been cultured overnight. Aggregates were incubated with bead mixture on a rocker for 40 min to allow for the dispersion of beads over aggregates. After incubation, aggregates were rinsed with Dulbecco's PBS to ensure that any excess beads were removed. Ceramic magnets (Dura Magnetics, Sylvania, OH) were placed atop the petri dishes. The magnetic field (618 G) produced by the magnets pulled on the microbeads and exerted an upward force (173 pN) on the cellular aggregates. Control cells without magnetic microbeads were cultured within the magnetic field as well as additional control samples cultured with magnetic microbeads, but not under a magnetic field. Samples were allowed to incubate underneath the magnets for 1 week.

RESULTS AND DISCUSSION

Homogeneous models predict high stresses and low traction forces in the center of multicellular aggregates

Microcontact printing, a technique used to pattern protein shapes onto cell culture surfaces, is frequently used to create confined shapes for single cells and multicellular assemblies to examine the effects of geometric constraint on cell phenotype and fate (1-3,6). In this study, we cultured groupings of fibroblastic cells (porcine VICs) onto 200–400 μm diameter circular collagen micropatterns on controlled-stiffness polyacrylamide gels. Each multicellular aggregate contained 100-200 cells in a monolayer that were able to interact with the substrate and other neighboring cells. Traction stresses in the substrate were studied via displacement of fluorescent beads to understand cell interactions by region.

To determine the cell-layer stresses within aggregates, we performed two different types of modeling: a forward-predicting thermal contraction model pioneered by Chen and colleagues (1) and a direct calculation of stresses using MSM developed by Fredberg and colleagues (23). For the thermal contraction model, we induced homogeneous contraction by setting a uniform coefficient of thermal expansion throughout the cell layer and applying a simulated temperature drop per the methods of Li and colleagues (2). We found that predicted traction stresses in the substrate below the cell layer are highest along the aggregate edge and lowest in the center (Fig. 1 a), which agrees with previous findings (1,2,9). The predicted average normal stress $((\sigma_1 + \sigma_2)/2$, where σ is principal stress) in the cell layer has the opposite trend, with normal cell stress low at the edge and high in the center (Fig. 1 b).

For our homogeneous MSM model, experimentally measured traction forces were applied to the lower surface of a finite element model with uniform modulus throughout the cell layer based on the methods of Ji and colleagues (Fig. 1 c; (6)). These directly measured traction forces were averaged from six different aggregates to create a representative aggregate with a radially symmetric prototypical traction force distribution. On average, traction forces were highest at the edge and lowest in the center, as seen in previous studies (6,16). For the homogeneous model, the calculated average normal stresses are highest in the center and lowest along the edge (Fig. 1 d) in agreement with previous predictions and calculations for constrained cell layers (7,23).

In contrast to these homogeneous model predictions and calculations, high cell stress associated biomarkers including cell spreading (19), elongation (7), α -smoothmuscle-actin (α -SMA)-rich stress fibers (24), proliferation (1), and traction force generation (2,16) have all been reported at the edges of constrained multicellular aggregates.

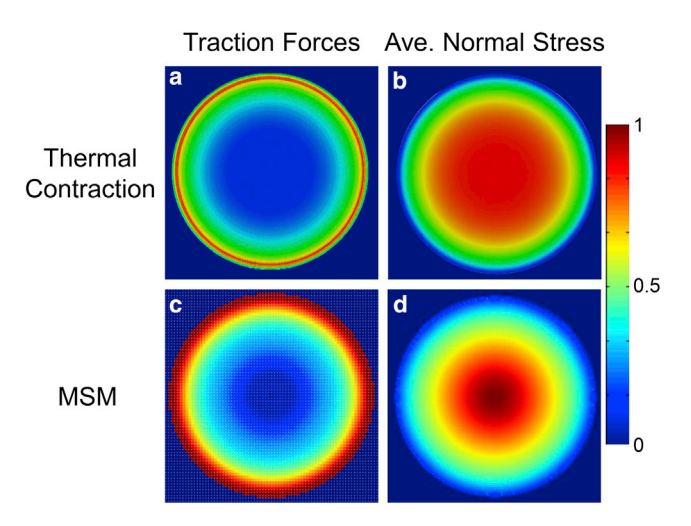


FIGURE 1 Homogeneous thermal contraction and MSM modeling reveal high cell stress in the aggregate center and high tractions at the edge. Heat maps of traction forces for homogeneous thermal contraction (a) and MSM model (c) show high tractions along the aggregate periphery. Heat maps of cell-layer stress for homogeneous thermal contraction (b) and the MSM model (d) display high stresses in the aggregate center. To see this figure in color, go online.

The homogenous models may be applicable to justconfluent layers and freely expanding monolayers where cell density remains relatively uniform. However, it appears that when cell populations grow within geometrically constrained areas, cell density increases nonuniformly and cell behavior changes regionally (25). We posit that when this nonuniform behavior occurs, the assumption of homogeneity is no longer valid.

Distributions of high-stress biomarkers localize to aggregate periphery

To obtain more refined distributions of mechanical stressrelated biomarkers, we quantified two cytoskeletal markers associated with cell contractility: α -SMA, the hallmark of the contractile myofibroblast phenotype (26), and the ratio of globular actin (G-actin) to F-actin. Additionally, the distributions of two mechanosensitive indicators of cell fate were analyzed: apoptosis (27,28) and yes-associated protein (YAP) nuclear localization (4,29,30).

Incorporation of α -SMA into stress fibers correlates with the increase in contractile force in populations of fibroblasts cultured in 3D protein gels (31) and on compliant gels (24). We observed a doubling of α -SMA intensity and incorporation into stress fibers from the center to the periphery in our patterned aggregates (Fig. 2 a), which agrees with previous studies of patterned fibroblasts assemblies (2). Under tension, F-actin stress fibers polymerize G-actin monomer units, thereby increasing the persistence length of fibers, whereas unloaded F-actin filaments depolymerize into G-actin (32). If the total actin within a cell is conserved, G-/F-actin ratios should be high for cells under low cell stress. We observed high G-/F-actin ratio values in the center and low values at the edge further indicating lower celllayer stress in central regions compared to the periphery (Fig. 2b).

Previous evidence indicates that cells require a basal level of homeostatic tension to survive and that apoptosis is linked to states of low cell stress (33,34). Increased rates of apoptosis have been found in single cells restricted in spreading by culturing on small protein islands (<20 µm diameter) (35) in adherence-dependent cells that are detached from a substrate (termed anoikis) (36) and in cells cultured on soft substrates (37). In our multicellular aggregates, the predominant apoptotic activity occurs in the aggregate center and decreases toward the aggregate edge (Fig. 2 c). Additionally, compared to central cells, peripheral cells create larger, more persistent F-actin fibers, have higher fiber alignment, and align more circumferentially, indicating anisotropic stress (Fig. 2, d and e).

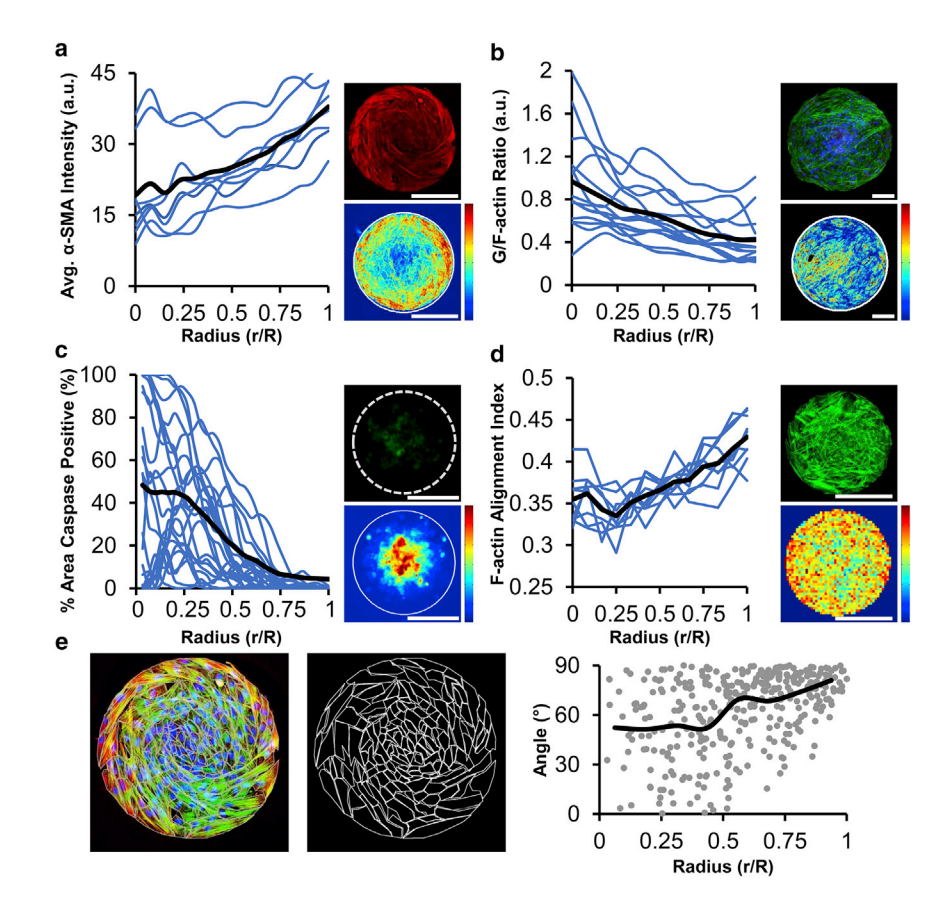


FIGURE 2 Protein measurements for cell-layer stress indicate low stress state within the center of VIC aggregates. (a) α -SMA intensity doubles from the center to edge of the aggregate. The inset shows the aggregate stained for α -SMA (top; red) and a heat map of average (Avg.) α -SMA intensity (bottom). n = 8 images (two replicates). (b) G-/Factin ratio with respect to the aggregate radius decreases from the center to periphery. The inset shows the aggregate (top) stained for F-actin (green), G-actin (red), and nuclei (blue) and a heat map of average G-/F-actin intensity (bottom). n = 14 images (3 replicates). (c) Cleaved caspase-3/7 presence decreases from the center to edge of the aggregate. The inset shows the aggregate stained for caspase-3/7 (top; green, dotted line indicates the aggregate edge). A heat map was generated for the average caspase-3/7 intensity (bottom). n = 24 images (1 replicate). (d) F-actin alignment index increases from the center to edge of the aggregate. An index of zero indicates no stress fiber alignment, whereas an index of one indicates perfect fiber alignment. The inset shows the aggregate stained for F-actin (top; green) and a heat map for average alignment index (bottom). n = 9images (two replicates). (e) The left panel shows the aggregate with individual cells outlined and measured for cell angle. The center panel shows individual cell outlines. The right panel showing the angle of cell in relation to the radial angle (90° indicates perpendicular to radial angle) shows that peripheral cells circumferentially align more than central cells. n = 2 images (two replicates). Scale bars, $100 \mu m$. To see this figure in color, go online.

Restricting cell contractility by culturing cells at high density, culturing cells on low modulus substrates, or inhibiting contractility with ROCK inhibitors results in cytoplasmic YAP localization (38). In our aggregates, we observe YAP nuclear exclusion within central cells and nuclear localization in peripheral cells (Fig. S5). Combined, these distributions of stress-related biomarkers strongly suggest that low cell-layer stress occurs within the center of constrained multicellular aggregates, whereas edge cells generate relatively high anisotropic internal stress.

Similar to our micropatterned cell layers, in geometrically constrained multicellular systems in vivo (e.g., the Drosophila wing), increased proliferation along the edge region increases crowding of central cells and reduces cell spread area (39). Constrained cell growth induces compression on central cells leading to apoptosis (40,41). This major difference in cell behavior with respect to wing location suggests that the local environment sensed by cells is nonuniform. This dynamic phenomenon requires heterogeneous parameters to accurately predict cell-layer stresses.

Central cells vary in morphology, behavior, and properties compared to peripheral cells

It is well established that cell-generated forces increase with increasing spread area (22,37-39). To obtain a rough estimate of the radial variation of contractility of the cells within our aggregates, we first determined a relationship between cell spread area and radius within aggregates (Area = A(r)) by outlining individual cells within one aggregate. We found that cells elongated along the periphery had spread areas approximately eight times larger than centrally located cells (Fig. 3, a and b). We then segmented aggregates into two regions (center: $0 \le r < 0.5R$ and periphery: $0.5R \le r \le R$, where r = radius and R = max radius) and calculated the average spread area for each region over time. After 1 day postconfluence, the average cell spread area in the central region was $\sim 50\%$ of peripheral cells (Fig. 3 c). In contrast, Ji and colleagues (7) report uniform cell area of MC3T3 cells regardless of their position on circular and ring-shaped micropatterns. This discrepancy may be due to their experimental timing being immediately at confluence rather than after cell crowding. In confluent cell layers on constrained patterns, cells proliferate at the edge (1,2,4) and then migrate inward, causing crowding in the center. After 1 week postconfluence in our aggregates, the average cell spread area decreases by more than 50% in both central and peripheral regions (Fig. 3 c). The increase in cell number over time results in smaller average spread areas in aggregate centers, decreasing to constrained single cell sizes previously shown to induce apoptosis (35).

Next, we established a quantitative relationship between cell-generated traction forces and cell spread area (Force = F(A)) by measuring traction forces of individual VICs on 7.5 kPa polyacrylamide gels (Fig. 3 d). Similar to previous findings (21,22,42), we observed a positive linear relationship between traction forces and spread area and also between maximum substrate stress and spread area. On

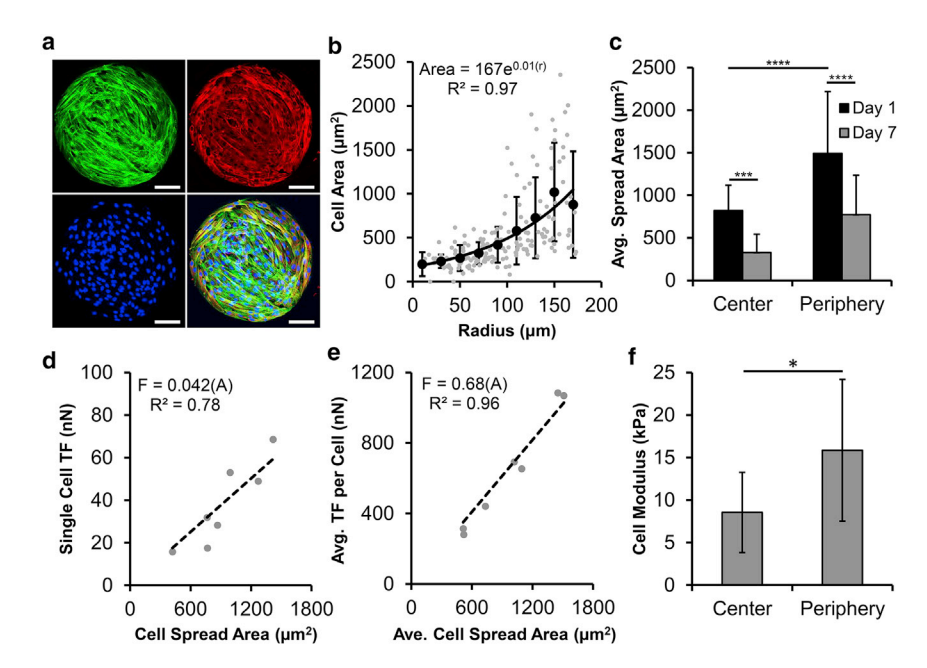


FIGURE 3 Cells within the central region of aggregates have on average, lower spread area, lower traction force (TF), and lower indentation stiffness compared to those in the peripheral area. (a) Aggregate stained for F-actin (green), α-SMA (red), nuclei (blue), and merge is shown. Scale bars, 50 μ m. (b) The measured relationship for cell area as a function of radius for one aggregate is shown. Gray dots are raw data, black dots are mean ± standard deviation for 20 μ m bins, and the exponential trendline is fit to binned means. (c) The central cell spread area is approximately half that of peripheral cells. Cell spread area decreases over 1 week in culture in both central and peripheral regions. n = 22 cells for both the center and periphery at day 1, and N = 16 cells for both the center and periphery at day 7 (two replicates). Data are represented as mean ± standard deviation. *** indicates p < 0.001 and **** indicates p < 0.0001 for two-way analysis of variance with Sidak's post hoc test. (d) The relationship for TF as a function of cell area for individual VICs is shown. (e) The relationship of average TF as a function of average area per cell in multicellular aggregates is shown. (f) Central cells in aggregates have a lower modulus from AFM indentation analysis than peripheral cells. n = 8 aggregates (three replicates). Data are represented as mean \pm standard error, and * indicates p < 0.05 for Student's *t*-test. To see this figure in color, go online.

softer substrates, the cells generate even lower forces, yet a linear relationship between traction force and cell area remains. In multicellular aggregates, traction stresses exert local forces to neighboring cells and transfer forces between them. Traction stresses and strain energy increase with individual cell or multicellular aggregate size, localize along the cell or aggregate periphery, and are independent of the number of cells present (22,43). Further, during the seeding process, natural variation occurs in the number of cells that attach to any given protein pattern. Similar to Dufresne and colleagues (43), we found that total traction force generated by a multicellular colony scales with the total area of the colony yet is surprisingly insensitive to the number of cells present. Thus, the average traction force per cell in an aggregate (total aggregate traction force divided by number of cells) decreases with increased cell density in multicellular aggregates (Fig. 3 e). Combined, these results strongly suggest that within saturation limits, cells generate traction forces roughly proportional to their spread area over a large range of areas, regardless of whether the cells are isolated or in multicellular aggregates. This behavior forms the basis for how we model contractility with respect to radius in our heterogeneous model.

The cell stiffness also appears to follow the trend of cell area. Using AFM stiffness mapping, we observed stiffness values approximately half as large in central regions compared to peripheral regions in aggregates (Fig. 3 f). Indentation stiffness measured by AFM is related to both the intrinsic modulus of cells and the level of tension in their cytoskeletons (44). Together, these results demonstrate that central cells have smaller spread areas, generate lower tension, and have lower cell moduli compared to peripheral cells.

Heterogeneous models predict stress distributions inverse to homogeneous models

To predict the cell-layer stress within aggregates, we induced contraction in our finite element model with a simulated temperature drop (2). In the homogeneous case (uniform coefficient of thermal expansion), cell-layer stress increases from the edge to the center as previously reported for similar simulations (1,2,6). For our heterogenous model, we approximated contractility as a continuous exponential heterogeneous distribution based on experimentally measured data. Alternatively, we utilized a heterogeneous step function that gives results comparable to the exponential distribution but is less realistic (Fig. S6). However, it allows a clearer visualization of how the stresses change with an abrupt change in properties. Our step-function heterogeneous model results in stress distributions consistent with Edwards and Schwarz (45), who show a sudden change in stress at the transition point between the two values of contractility. Using the linear regression of traction forces for individual cells and the exponential relationship between cell area and radius (see Fig. 3, b and d), we generated a quantitative relationship between traction force and radial location. In our model, we assumed that $\alpha(r)$ follows the same trend as $F(\mathbf{r})$, which provided us with the coefficient of thermal expansion as a function of radius ($\alpha(r)$ = $0.9e^{2.34r}$) and normalized to its initial value. The circumferential stress profile for this exponential heterogeneous case decreases 3.5-fold from the edge to the center (Fig. 4 a), which is the inverse of the homogeneous case in which the stress increases twofold. Additionally, the radial stress in the heterogeneous case is highest toward the edge and decreases by half toward the center. The stress predictions from the heterogeneous models match biological markers of cell-layer stress state far better than the homogeneous model.

Considering the roughly inverse patterns of cell-layer stress, predicted substrate traction stress patterns are surprisingly similar for the homogeneous and heterogeneous models (Fig. 4, b and c). In the heterogeneous cases, small positive (outward) tractions are generated in the center because of relatively high contraction of the peripheral region pulling on the central region. We found this result to be evident in some experimental traction force maps (Fig. S7). This phenomenon has also been reported in another study in which modeling contraction as a step change caused positive displacements (outward) to form even though the layer as a whole was retracting (45). These results demonstrate that variations in collective cell

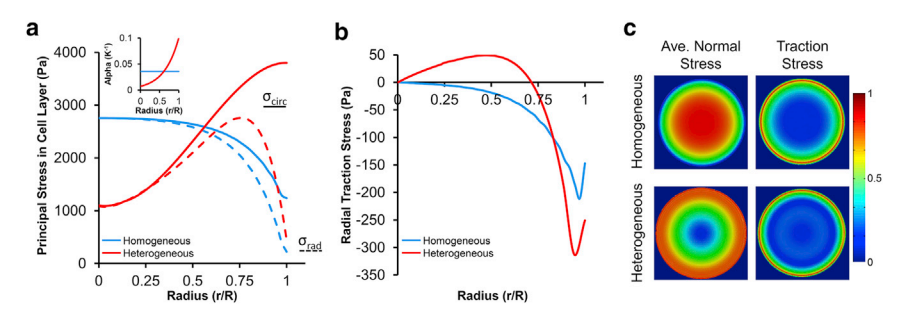


FIGURE 4 Continuous distribution for contractile stresses as a function of radius is used to simulate cell-layer and substrate stresses. (a) Shown are cell-layer radial (dotted) and circumferential (solid) stresses with homogeneous (blue) and exponential heterogeneous (red) conditions for contractility (coefficient of thermal expansion, α , is shown graphically at the top of b). (b) Predicted radial traction stresses for homogeneous (blue) and exponential heterogeneous (red) models of cell contractility as a function of radius are shown. (c) Heat maps of predicted average normal stress and traction stresses for the homogeneous and exponential conditions are shown. To see this figure in color, go online.

contractility greatly affect cell-layer stress distributions but have little effect on substrate traction stresses, which suggests that using accurate cell-layer mechanical properties is critical for accurately estimating cell-layer stresses from measured traction stresses.

MSM trends agree with thermal contraction models

We then directly calculated the in-plane stress distribution using MSM (6). We modeled the cell layer as a passive uniform-thickness linear elastic disk and applied measured substrate traction forces to the lower surface of the model (Fig. 5). In an approach analogous to the simulations, we calculated the stresses for three cases: homogeneous elastic modulus, step-function modulus (Fig. S8 a), and an exponentially increasing modulus $(E(r) = 0.9e^{2.34r})$ from the center to the edge. Similar to the coefficients of thermal expansion, these modulus values were normalized to have the same average value. Average stress values substantially decrease in central regions of aggregates and increase in the peripheral region when introducing heterogeneous conditions (Fig. 5).

The individual cell-layer stress patterns from each aggregate are nonuniform but different in magnitude and form. In all cases, the heterogeneous conditions had lower stresses in the center compared to the homogeneous case. Experimentally measured substrate stresses from six different aggregates were binned together with respect to their radial location from the center of the aggregate. An average traction force per radial bin was calculated and a best fit curve was fitted to represent any traction force for a given radius (Fig. 6 a). The equation for the best fit curve is as follows:

$$T(r) = (-7.01E - 8)r^{6} + (1.96E - 5)r^{5}$$
$$- (2.03E - 3)r^{4} + (9.52E - 2)r^{3}$$
$$- (1.93E)r^{2} + (1.62E + 1)r,$$
 (11)

where r is the radius, E is Young's modulus, and T(r) is the average traction stress in pascals. On average, the traction stress near the aggregate edge is high and then decreases

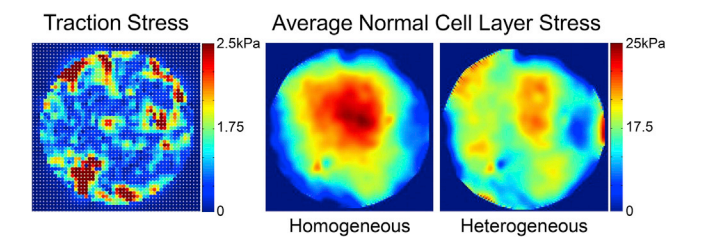


FIGURE 5 Heat maps from left to right show measured traction stresses and output average normal stresses for homogeneous and exponential models for a representative aggregate. Distributions of cell-layer elastic moduli are homogeneous and exponentially varying modulus per equation $E(r) = 0.9e^{2.34r}$. To see this figure in color, go online.

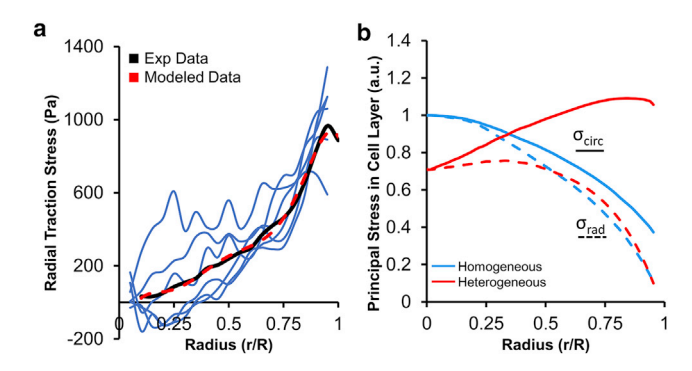


FIGURE 6 Cell-layer stresses calculated by MSM for homogeneous and heterogeneous conditions from traction forces averaged over many aggregates. (a) The average radial traction stresses measured from six aggregates (blue lines) were averaged (black line) and a best fit curve (red dashed) was determined. (b) Inputting average traction stresses versus radius generates predictive models for cell-layer radial (dotted) and circumferential (solid) stresses with homogeneous (blue) and exponential heterogeneous (red) conditions for modulus. To see this figure in color, go online.

toward the center. These average traction stresses were input into the three different case models to obtain radial and circumferential cell-layer stresses for an average aggregate using MSM (Figs. 6 b and S8 b).

In the homogeneous disk (uniform elastic modulus), both radial and circumferential stresses are highest in the center and decrease toward the edge. For the exponential function heterogeneous disk, radial stress increases rapidly from the edge and then levels out toward the center, whereas the circumferential stress is high at the edge and decreases toward the center (Fig. 6 b). The stress distributions calculated with the average tractions are similar to those simulated with the thermal contraction model (cf. Figs. 4 a and 6 b). These results further emphasize that cell-layer stress cannot be solely inferred from substrate tractions without additional specification of cell-layer material properties.

Interpretation of stress measurements relative to biological markers

In past studies, certain biomarkers have been related to regions of "high stress" that are predicted by computational models. In these cases, the authors refer to predicted substrate traction stresses, not cell-layer stress. Although it is possible that traction stresses drive some cell behaviors, it is more likely that many markers related to intracellular stresses are driven by the cell-layer stress state rather than substrate traction stresses. For example, when increasing stress in cell clusters via mechanical stretching, α -SMA increases throughout aggregates (2). Additionally, actin stress fiber formation, amounts of F-actin and G-actin, and proliferation markers are also likely related to be driven by the internal stress state within a cell. On the other hand, one biomarker that is likely dependent on traction stresses rather than cell-layer stress would be focal adhesion size. Focal adhesion size has previously been correlated to traction stress magnitude (46). These markers are found to be highest at cell cluster edges, yet homogeneous models predict highest stresses in the center.

When averaged over many postconfluent aggregates, stress-related biomarkers, such as α -SMA, F-actin, and traction forces, clearly localize to aggregate edges. However, when considering cases in which cells are able to move more independently, a large variability between aggregates has been observed. Large traction forces have been shown to accumulate in inner regions in aggregates below or at confluence and in aggregates with highly motile cells (47,48). Thus, the emergent cell behavior and stress distributions predicted by our models are likely only valid for postconfluent aggregates wherein heterogeneity in cell density is established because of the geometric constraints.

Previous studies have also utilized results from homogenous models to explain circumferential cell alignment near the edges of patterned multicellular systems. Ji and colleagues (6,7) attribute the alignment to stress anisotropy, defined by the difference in principal in-plane stresses (equivalent to twice the maximum in-plane shear stress). Cell alignment along the maximum principal stress direction is also found in other systems (49). Our heterogeneous models accentuate the anisotropy of stresses present at the edges while also predicting low magnitude average normal stresses in the center, which correspond to the high levels of apoptosis at the center. The biological factors that we measured are clear indicators of cellular stress, and it is therefore unlikely that anisotropy is the cause of the distribution of biomarkers but rather the cell-layer stress itself that is the main contributor.

To the best of our knowledge, all current models that calculate cell-layer stress use homogeneous models with the exception of Tambe et al. (15). In that study, the local elastic modulus was increased in proportion to the local stress that was precalculated assuming a homogeneous elastic modulus, and little change in the distribution of stresses was found. However, they focused on ruggedness of the stress landscape in migrating monolayers and did not consider geometrically constrained aggregates of proliferating cells. In contrast, our simulations decrease the contractility or modulus distribution from the edge to the center based on independent biophysical parameters, and we focus our attention on the distribution of stress magnitude and how this corresponds to certain biological responses.

To experimentally test whether the change in stress predicted by homogeneous or heterogeneous models is more likely the driver of the observed radial distribution in biomarkers, we increased the cell-layer stress in the central region by applying an external load using magnetic microbeads (50). Magnetic microbeads coated with collagen were uniformly deposited and attached to cultured cells and exposed to external loads via a magnetic force (Fig. S9 a). Over the course of 7 days, the magnetic beads accumulated in the central region of the aggregate, indicating migration of periphery cells to the center of the aggregates. Applying the magnetic force for 1 week decreased the apoptotic activity within aggregates and resulted in more uniform and diffuse α -SMA staining (Fig. S9, b and c). Application of the magnetic field also increased the nuclear aspect ratio for center cells such that they were equivalent to that of edge cells (Fig. S9 d). Together, these results suggest that the additional out-of-plane mechanical load in the center results in higher intracellular stress and therefore more uniform biological behavior across the aggregate, which supports the heterogeneous model. If the central region had initially higher stress than the edges, as predicted by the homogeneous model, the additional loading would enhance the differences in biomarkers from the center to edge.

CONCLUSIONS

In this study, we present experimental and computational evidence that incorporation of heterogeneity in regional cell properties is critical for accurate estimation of distributed cell-layer stresses. By incorporating heterogeneous cell contractility and mechanical parameters, our enhanced finite element model yields cell-layer stress contours that agree with multiple biological measures of local cell stress, all of which indicate low stress in the center of multicellular aggregates and high circumferentially aligned stress at the periphery. Homogeneous models may be sufficient for estimating stress distributions in unconstrained systems and/or for short culture times in which cell density remains constant. However, our results strongly suggest that in constrained systems over longer time frames, proliferation and growth lead to regional changes in cell shape, size, and physical properties that must be considered in mechanical analysis of multicellular systems.

SUPPORTING MATERIAL

Supporting Material can be found online at https://doi.org/10.1016/j.bpj. 2019.11.018.

AUTHOR CONTRIBUTIONS

Z.E.G., H.A. Cirka, and K.L.B. designed experiments. Z.E.G. and H.A. Cirka conducted biological experiments. H.A. Choshali performed modeling experiments. Z.E.G., H.A. Choshali, and H.A. Cirka analyzed data. V.L. contributed data. Q.W. and D.M. helped with experimental methods. N.R. helped with modeling methods. Z.E.G., H.A. Choshali, Q.W., D.M., N.R., and K.L.B. interpreted the data. Z.E.G., H.A. Cirka, and K.L.B. wrote the manuscript.

ACKNOWLEDGMENTS

Will Linthicum is acknowledged for his help and expertise with the AFM experiments.

This work was funded in part by grants from the National Science Foundation (CMMI 1761432), the National Institutes of Health (2R15HL087257-02A1), and a Worcester Polytechnic Institute/University of Massachusetts Medical School Seed Grant. This work was also funding in part by the National Science Foundation IGERT (DGE 1144804) for H.A. Cirka and Z.E.G. and the American Heart Association Predoctoral Fellowship for H.A. Cirka (14PRE18310016).

REFERENCES

- Nelson, C. M., R. P. Jean, ..., C. S. Chen. 2005. Emergent patterns of growth controlled by multicellular form and mechanics. *Proc. Natl. Acad. Sci. USA*. 102:11594–11599.
- Li, B., F. Li, ..., J. H. Wang. 2009. Spatial patterning of cell proliferation and differentiation depends on mechanical stress magnitude. J. Biomech. 42:1622–1627.
- Wan, L. Q., S. M. Kang, ..., G. Vunjak-Novakovic. 2010. Geometric control of human stem cell morphology and differentiation. *Integr. Biol.* 2:346–353.
- Aragona, M., T. Panciera, ..., S. Piccolo. 2013. A mechanical checkpoint controls multicellular growth through YAP/TAZ regulation by actin-processing factors. Cell. 154:1047–1059.
- Lee, J., A. A. Abdeen, ..., K. A. Kilian. 2016. Interfacial geometry dictates cancer cell tumorigenicity. *Nat. Mater.* 15:856–862.
- Liu, C., S. He, ..., B. Ji. 2016. Mechanics of cell mechanosensing on patterned substrate. J. Appl. Mech. 83:1–8.
- He, S., C. Liu, ..., B. Ji. 2015. Dissecting collective cell behavior in polarization and alignment on micropatterned substrates. *Biophys. J.* 109:489–500.
- 8. Brugués, A., E. Anon, ..., X. Trepat. 2014. Forces driving epithelial wound healing. *Nat. Phys.* 10:683–690.
- Banerjee, S., and M. Cristina Marchetti. 2013. Controlling cell-matrix traction forces by extracellular geometry. New J. Phys. 15:035015.
- Trepat, X., M. R. Wasserman, ..., J. J. Fredberg. 2009. Physical forces during collective cell migration. *Nat. Phys.* 5:426–430.
- Moussus, M., C. der Loughian, ..., A. Nicolas. 2014. Intracellular stresses in patterned cell assemblies. Soft Matter. 10:2414–2423.
- Maruthamuthu, V., B. Sabass, ..., M. L. Gardel. 2011. Cell-ECM traction force modulates endogenous tension at cell-cell contacts. *Proc. Natl. Acad. Sci. USA*. 108:4708–4713.
- Nier, V., S. Jain, ..., P. Marcq. 2016. Inference of internal stress in a cell monolayer. *Biophys. J.* 110:1625–1635.
- Ng, M. R., A. Besser, ..., G. Danuser. 2014. Mapping the dynamics of force transduction at cell-cell junctions of epithelial clusters. *eLife*. 3:e03282.
- Tambe, D. T., U. Croutelle, ..., J. J. Fredberg. 2013. Monolayer stress microscopy: limitations, artifacts, and accuracy of recovered intercellular stresses. *PLoS One*. 8:e55172.
- Cirka, H. A., J. Uribe, ..., K. L. Billiar. 2017. Reproducible in vitro model for dystrophic calcification of cardiac valvular interstitial cells: insights into the mechanisms of calcific aortic valvular disease. *Lab Chip.* 17:814–829.
- Gould, R. A., and J. T. Butcher. 2010. Isolation of valvular endothelial cells. J. Vis. Exp. 46:6–10.
- Throm Quinlan, A. M., L. N. Sierad, ..., K. L. Billiar. 2011. Combining dynamic stretch and tunable stiffness to probe cell mechanobiology in vitro. PLoS One. 6:e23272.
- Cirka, H., M. Monterosso, ..., K. Billiar. 2016. Active traction force response to long-term cyclic stretch is dependent on cell pre-stress. *Biophys. J.* 110:1845–1857.
- Kilian, K. A., B. Bugarija, ..., M. Mrksich. 2010. Geometric cues for directing the differentiation of mesenchymal stem cells. *Proc. Natl. Acad. Sci. USA*. 107:4872–4877.

- Rape, A. D., W. H. Guo, and Y. L. Wang. 2011. The regulation of traction force in relation to cell shape and focal adhesions. *Biomaterials*. 32:2043–2051.
- 22. Oakes, P. W., S. Banerjee, ..., M. L. Gardel. 2014. Geometry regulates traction stresses in adherent cells. *Biophys. J.* 107:825–833.
- Tambe, D. T., C. C. Hardin, ..., X. Trepat. 2011. Collective cell guidance by cooperative intercellular forces. *Nat. Mater.* 10:469– 475
- Chen, J., H. Li, ..., J. H. C. Wang. 2007. Alpha-smooth muscle actin expression enhances cell traction force. *Cell Motil. Cytoskeleton*. 64:248–257.
- Zimmermann, J., B. A. Camley, ..., H. Levine. 2016. Contact inhibition of locomotion determines cell-cell and cell-substrate forces in tissues. *Proc. Natl. Acad. Sci. USA*. 113:2660–2665.
- Hinz, B. 2010. The myofibroblast: paradigm for a mechanically active cell. *J. Biomech.* 43:146–155.
- Desouza, M., P. W. Gunning, and J. R. Stehn. 2012. The actin cytoskeleton as a sensor and mediator of apoptosis. *Bioarchitecture*. 2:75–87.
- Gourlay, C. W., and K. R. Ayscough. 2005. The actin cytoskeleton: a key regulator of apoptosis and ageing? *Nat. Rev. Mol. Cell Biol.* 6:583–589.
- Das, A., R. S. Fischer, ..., C. M. Waterman. 2016. YAP nuclear localization in the absence of cell-cell contact is mediated by a filamentous actin-dependent, myosin II- and phospho-YAP-independent pathway during extracellular matrix mechanosensing. *J. Biol. Chem.* 291:6096–6110.
- Elosegui-Artola, A., I. Andreu, ..., P. Roca-Cusachs. 2017. Force triggers YAP nuclear entry by regulating transport across nuclear pores. Cell. 171:1397–1410.e14.
- Hinz, B., G. Celetta, ..., C. Chaponnier. 2001. Alpha-smooth muscle actin expression upregulates fibroblast contractile activity. *Mol. Biol. Cell.* 12:2730–2741.
- dos Remedios, C. G., D. Chhabra, ..., N. J. Nosworthy. 2003. Actin binding proteins: regulation of cytoskeletal microfilaments. *Physiol. Rev.* 83:433–473.
- Egerbacher, M., S. P. Arnoczky, ..., K. L. Gardner. 2008. Loss of homeostatic tension induces apoptosis in tendon cells: an in vitro study. Clin. Orthop. Relat. Res. 466:1562–1568.
- Humphrey, J. D., E. R. Dufresne, and M. A. Schwartz. 2014. Mechanotransduction and extracellular matrix homeostasis. *Nat. Rev. Mol. Cell Biol.* 15:802–812.
- Chen, C. S., M. Mrksich, ..., D. E. Ingber. 1997. Geometric control of cell life and death. Science. 276:1425–1428.
- Frisch, S. M., and E. Ruoslahti. 1997. Integrins and anoikis. Curr. Opin. Cell Biol. 9:701–706.
- Wang, H. B., M. Dembo, and Y. L. Wang. 2000. Substrate flexibility regulates growth and apoptosis of normal but not transformed cells. *Am. J. Physiol. Cell Physiol.* 279:C1345–C1350.
- 38. Dupont, S. 2016. Role of YAP/TAZ in cell-matrix adhesion-mediated signalling and mechanotransduction. *Exp. Cell Res.* 343:42–53
- Legoff, L., H. Rouault, and T. Lecuit. 2013. A global pattern of mechanical stress polarizes cell divisions and cell shape in the growing *Drosophila* wing disc. *Development*. 140:4051–4059.
- Mao, Y., A. L. Tournier, ..., N. Tapon. 2013. Differential proliferation rates generate patterns of mechanical tension that orient tissue growth. *EMBO J.* 32:2790–2803.
- 41. Diaz de la Loza, M. C., and B. J. Thompson. 2017. Forces shaping the Drosophila wing. *Mech. Dev.* 144:23–32.
- Califano, J. P., and C. A. Reinhart-King. 2010. Substrate stiffness and cell area predict cellular traction stresses in single cells and cells in contact. *Cell. Mol. Bioeng.* 3:68–75.

- 43. Mertz, A. F., S. Banerjee, ..., E. R. Dufresne. 2012. Scaling of traction forces with the size of cohesive cell colonies. Phys. Rev. Lett. 108:198101.
- 44. Canović, E. P., D. T. Seidl, ..., D. Stamenović. 2014. Stiffness versus prestress relationship at subcellular length scale. J. Biomech. 47:3222–3225.
- 45. Edwards, C. M., and U. S. Schwarz. 2011. Force localization in contracting cell layers. Phys. Rev. Lett. 107:128101.
- 46. Goffin, J. M., P. Pittet, ..., B. Hinz. 2006. Focal adhesion size controls tension-dependent recruitment of α -smooth muscle actin to stress fibers. J. Cell Biol. 172:259-268.
- 47. Dumbali, S. P., L. Mei, ..., V. Maruthamuthu. 2017. Endogenous sheetaveraged tension within a large epithelial cell colony. J. Biomech. Eng. 139:101008.
- 48. Schaumann, E. N., M. F. Staddon, ..., S. Banerjee. 2018. Force localization modes in dynamic epithelial colonies. Mol. Biol. Cell. 29:2835-
- 49. Yuan, H., B. Marzban, and K. Kit Parker. 2017. Myofibrils in cardiomyocytes tend to assemble along the maximal principle stress directions. J. Biomech. Eng. 139:1210101-1210108.
- 50. Pinto, V. I., V. W. Senini, ..., C. A. McCulloch. 2014. Filamin A protects cells against force-induced apoptosis by stabilizing talin- and vinculin-containing cell adhesions. FASEB J. 28:453-